


Article

Adsorption of Carbon Dioxide, Methane, and Nitrogen on Zn(dcpa) Metal-Organic Framework

Rui P. P. L. Ribeiro , Isabel A. A. C. Esteves  and José P. B. Mota *

LAQV-REQUIMTE, Department of Chemistry, NOVA School of Science and Technology, NOVA University of Lisbon, 2829-516 Caparica, Portugal; i.esteves@fct.unl.pt

* Correspondence: rpp.ribeiro@fct.unl.pt (R.P.P.L.R.); pmota@fct.unl.pt (J.P.B.M.)

Abstract: Adsorption-based processes using metal-organic frameworks (MOFs) are a promising option for carbon dioxide (CO₂) capture from flue gases and biogas upgrading to biomethane. Here, the adsorption of CO₂, methane (CH₄), and nitrogen (N₂) on Zn(dcpa) MOF (dcpa (2,6-dichlorophenylacetate)) is reported. The characterization of the MOF by powder X-ray diffraction (PXRD), thermogravimetric analysis (TGA), and N₂ physisorption at 77 K shows that it is stable up to 650 K, and confirms previous observations suggesting framework flexibility upon exposure to guest molecules. The adsorption equilibrium isotherms of the pure components (CO₂, CH₄, and N₂), measured at 273–323 K, and up to 35 bar, are Langmuirian, except for that of CO₂ at 273 K, which exhibits a stepwise shape with hysteresis. The latter is accurately interpreted in terms of the osmotic thermodynamic theory, with further refinement by assuming that the free energy difference between the two metastable structures of Zn(dcpa) is a normally distributed variable due to the existence of different crystal sizes and defects in a real sample. The ideal selectivities of the equimolar mixtures of CO₂/N₂ and CO₂/CH₄ at 1 bar and 303 K are 12.8 and 2.9, respectively, which are large enough for Zn(dcpa) to be usable in pressure swing adsorption.

Keywords: Zn(dcpa); MOF; framework flexibility; adsorption; gas storage; biogas; carbon capture



Citation: Ribeiro, R.P.P.L.; Esteves, I.A.A.C.; Mota, J.P.B. Adsorption of Carbon Dioxide, Methane, and Nitrogen on Zn(dcpa) Metal-Organic Framework. *Energies* **2021**, *14*, 5598. <https://doi.org/10.3390/en14185598>

Academic Editor: Francesco Frusteri

Received: 11 August 2021

Accepted: 3 September 2021

Published: 7 September 2021

Publisher's Note: MDPI stays neutral with regard to jurisdictional claims in published maps and institutional affiliations.



Copyright: © 2021 by the authors. Licensee MDPI, Basel, Switzerland. This article is an open access article distributed under the terms and conditions of the Creative Commons Attribution (CC BY) license (<https://creativecommons.org/licenses/by/4.0/>).

1. Introduction

Metal-organic frameworks (MOFs) are being touted as the next generation materials for several adsorptive separation and purification processes [1,2]. MOFs are porous crystalline materials consisting of metal centers connected by organic moieties [3]. An unlimited amount of MOF structures can be envisioned and perhaps synthesized; furthermore, the materials can be tailored for specific applications through pore size tuning and functionalization [4]. These features place MOFs as a very diverse class of materials with potential applications in nearly all fields of chemical engineering [5–12].

Among the available portfolio of MOFs, there are several structures that present structural flexibility, which can be triggered by exposure to specific guest species, changes in temperature or mechanical pressure, or interactions with light or electric fields [13,14]. Framework flexibility generally manifest itself through breathing or gate-opening effects [13]. A comprehensive review regarding MOF flexibility was published by Schneemann et al. [14], in which it is stated that, so far, less than a hundred MOFs have shown important breathing effects. The authors classified the type of flexibility into “breathing”, “swelling”, “linker rotation”, and “subnetwork displacement”. The most well-known cases of MOF flexibility are the breathing behavior of MIL-53 [15–17] and the gate-opening of ZIF-8 [18,19].

The MIL-53 family of MOFs consists of trivalent metal (e.g., Al [20], Cr [17], Fe [21], and Sc [22]) terephthalates, which can switch between large-pore (lp) and narrow-pore (np) forms [15–17], with unit cell volume variation of up to 40% [23]. The conformational change can be triggered by different stimuli, for example temperature changes [22,24], application of mechanical pressure [25,26], and adsorption of guest molecules (such as

H₂O, CO₂, and other gases) [20,22,26,27]. Interestingly, the synthesis route and solvents employed critically impact the breathing properties of MIL-53 [28], and several authors have observed the absence of the breathing effect in the commercial MIL-53(Al) synthesized by BASF (Basolite©A100) when exposed to CO₂ [29–31].

Another type of MOF flexibility is related to linker rotation [32], of which the most well-known example occurs in ZIF-8, which presents a gate-opening effect [18,19]. The linker rotation triggers a window opening that allows for the adsorption of larger molecules than expected [18].

Recently, MOFs with step-shaped isotherms typical of flexible MOFs have been considered as potential adsorbents for CO₂ capture by temperature swing adsorption (TSA), as they permit decreasing the energy consumption of the process when compared with traditional zeolite 13X systems [33].

Zn(dcpa) is a poorly studied microporous MOF that reportedly exhibits dynamic behavior and stepwise adsorption. Zn(dcpa) is based on paddle-wheel Zn₂ units and unsymmetrical pyridyl dicarboxylate, which give rise to a three-dimensional intersecting pore network with a pore opening of $6.3 \times 12.2 \text{ \AA}^2$ [34]. The Zn(dcpa) framework structure is shown in Figure 1. Liu et al. [34] observed the dynamic behavior of Zn(dcpa) upon exposure to N₂ and CO₂ at 77 K and 195 K, respectively. However, they did not observe the MOF's flexible behavior when adsorbing CO₂ at 273 and 293 K and N₂ at 293 K, up to 1 bar.

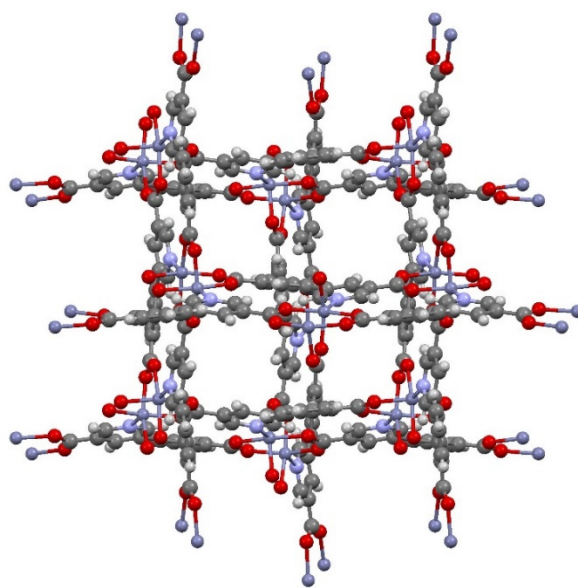


Figure 1. View of the Zn(dcpa) framework along the c-axis (Zn: blue, O: red, C: grey, and H: white). Data generated from the CIF file reported by Liu et al. [34].

In this work, the potential of Zn(dcpa) for application in the separation/purification of gaseous streams containing CO₂, CH₄, and N₂, namely post-combustion CO₂ capture and biogas upgrading, is evaluated. For this purpose, the single-component adsorption equilibria of CO₂, CH₄, and N₂ have been measured at 273–323 K up to 35 bar, and the isosteric heat of adsorption and ideal CO₂/CH₄ and CO₂/N₂ equilibrium selectivities evaluated. Furthermore, the MOF has been characterized regarding its textural properties and thermal stability. The uncommon stepwise adsorption and hysteretic desorption behavior for CO₂ at 273 K has been interpreted in terms of the osmotic thermodynamic theory. The data reported here add important knowledge about the adsorption properties of Zn(dcpa), as prior studies about this MOF are limited to a few publications [34,35].

2. Materials and Methods

2.1. Materials

The Zn(dcpa) MOF sample employed was synthesized at the Materials Center at Technical University Dresden (Germany). After its synthesis, the sample was washed with DMF and, subsequently, activated at 453 K under vacuum for 24 h. The gases employed in the measurements were provided by Air Liquide and Praxair (Portugal) with purities of 99.998% (CO₂), 99.95% (CH₄), 99.99% (N₂), and 99.999% (He).

2.2. Zn(dcpa) Characterization

The sample was characterized using powder X-ray diffraction (PXRD), thermogravimetric analysis (TGA), N₂ physisorption at 77 K, and helium porosimetry. The N₂ adsorption isotherm at 77 K and PXRD were determined by the supplier upon request. TGA analysis was performed using a LABSYS Evo TGA-DTA/DSC from SETARAM Instrumentation, under an argon flow at a heating rate of 3 K/min (up to 1130 K). Helium pycnometry was performed at 323 K, in a gravimetric apparatus (described in the next section), to determine the skeletal density of the MOF (ρ_s).

2.3. Single-Component Adsorption Equilibrium

Single-component adsorption equilibrium isotherms of CO₂, CH₄, and N₂ at 273 K, 303 K, and 323 K, between 0 and 35 bar, were determined using the standard static gravimetric method [31,36,37]. The measurements were performed in a high-pressure magnetic-suspension balance ISOSORP 2000 (Rubotherm GmbH, Germany) using approximately 600 mg of Zn(dcpa) powder. Both the adsorption and desorption data were recorded to evaluate the hysteretic effects. The sample was received from the supplier already activated and stored in an argon atmosphere, which is why the pre-treatment performed before measuring the adsorption equilibrium isotherms was limited to overnight vacuum. The experimental setup and procedure are detailed elsewhere [31,37].

The excess amount adsorbed, q_{exc} , is determined as follows

$$q_{exc} = \frac{w - m_s - m_h + V_h \rho_g}{m_s} + v_s \rho_g \quad (1)$$

where w is the apparent mass weighted; m_s is the mass of MOF; V_h and m_h correspond to the volume and mass of the measuring cell, respectively, which contribute to the buoyancy effects; ρ_g is the density of the bulk gas at the experimental conditions; and v_s is the specific volume of the solid matrix of the MOF ($v_s = 1/\rho_s$, where ρ_s is the skeletal density of the adsorbent). v_s was determined by helium pycnometry performed at 323 K in the gravimetric apparatus. This was determined assuming that He penetrates the MOF pore volume without being adsorbed.

The absolute amount adsorbed, q , can be determined from the excess amount adsorbed, using the following

$$q = q_{exc} \left(\frac{\rho_l}{\rho_l - \rho_g} \right) \quad (2)$$

assuming that the adsorbed phase density corresponds to the density of the liquid at its boiling point at 1 atm (ρ_l) [38].

3. Results and Discussion

3.1. Zn(dcpa) Characterization

The PXRD patterns obtained are displayed in Figure 2, showing that the position of the reflexes changed during activation. This effect was also observed by Liu et al. [34], who associated it with framework shrinkage upon removal of the guest molecules. The authors also observed the reversibility of this phenomenon when re-adsorbing the solvent.

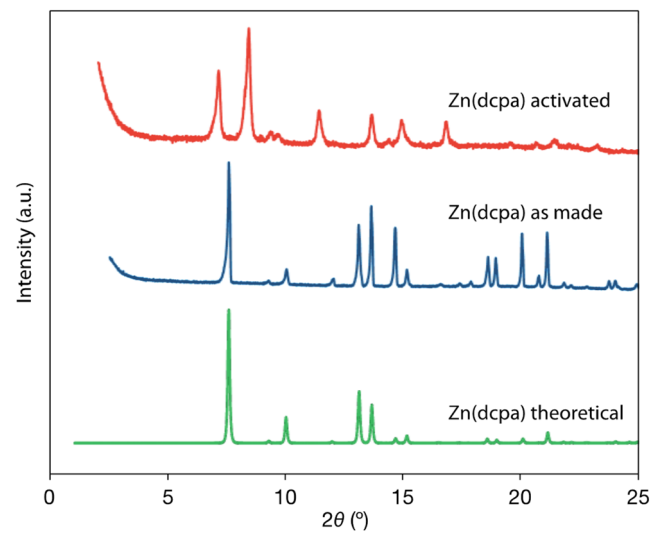


Figure 2. PXRD diffraction pattern for activated, as made, and theoretical Zn(dcpa) samples.

The thermal stability of the sample was also characterized by TGA; the recorded sample mass as a function of the heating temperature is shown in Figure 3. The results show an initial mass decrease ($\sim 10\%$) from room temperature up to around 400 K, due to the removal of pre-adsorbed impurities and humidity, due to MOF exposure to the indoor atmosphere just prior to the analysis. MOF was stable up to 650 K, after which a steep decrease in the mass was observed, reaching a mass decrease of 50%, similar to the behavior observed by Liu et al. [34]. Above 750 K, the Zn(dcpa) mass decreased more smoothly until reaching the remaining experimental amount of ca. 25% at 1130 K.

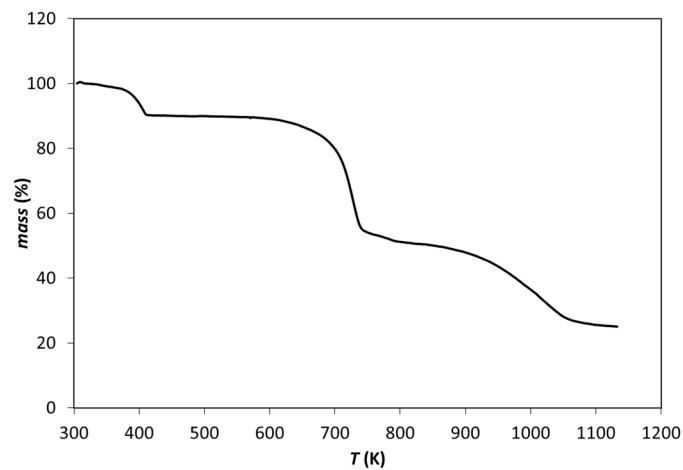


Figure 3. TGA results for Zn(dcpa) as a function of temperature (heating rate of 3 K/min).

The Zn(dcpa) porosity was evaluated by N_2 adsorption at 77 K. The obtained isotherm is plotted in Figure 4, showing an initial step followed by a smoother increase until $p/p_0 = 0.06$; then, another step increase is observed before reaching a nearly constant plateau with only a small increase between $p/p_0 = 0.2$ ($274 \text{ cm}^3/\text{g}$) and $p/p_0 = 0.97$ ($303 \text{ cm}^3/\text{g}$). Note that p and p_0 are the equilibrium and saturation pressures of the adsorbate at 77 K, respectively. The same behavior was observed by Liu et al. [34] who attributed the first step of the isotherm to the Zn(dcpa) structure with shrunken pores, and the second step to an expanded structure. In our work, the expanded structure had a specific pore volume of $0.47 \text{ cm}^3/\text{g}$, determined at a relative pressure of $p/p_0 = 0.97$, assuming the pores were filled with condensed liquid N_2 at its normal boiling point. The desorption branch showed hysteresis at $p/p_0 < 0.2$, which is also in accordance with a previous report, although in our case, the hysteresis loop seemed to close at lower

pressures—which corresponds to a return to the shrunken pore conformation—as opposed to the observation of Liu et al. [34].

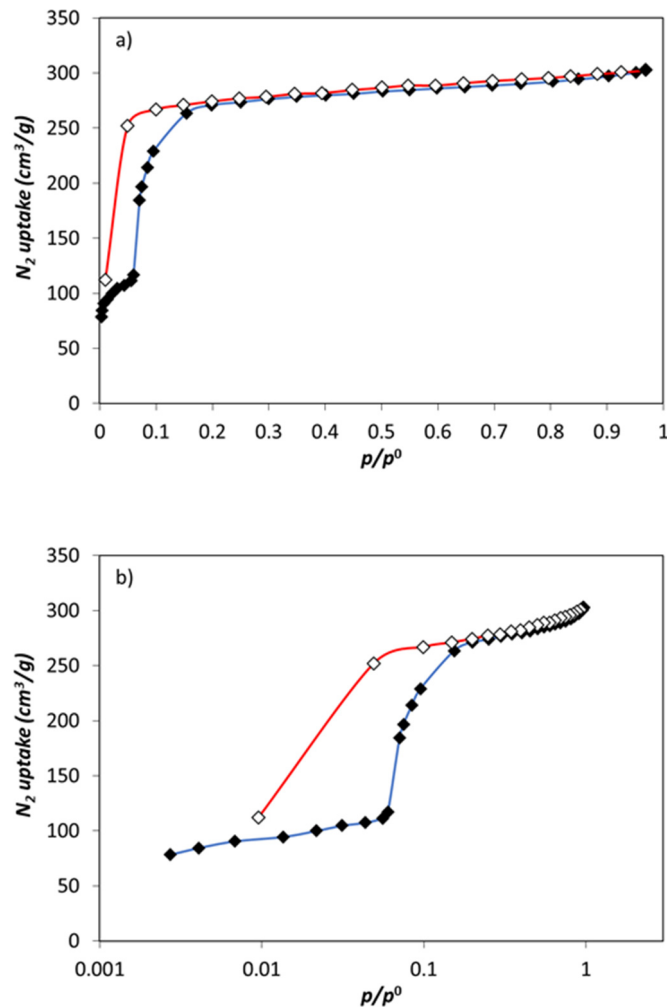


Figure 4. N_2 adsorption equilibrium isotherm at 77 K on Zn(dcpa) in linear (a) and log (b) scales. Filled and empty symbols represent the adsorption and desorption data, respectively.

3.2. Single-Component Adsorption Equilibrium

Prior to the adsorption of CO_2 , CH_4 , and N_2 , the skeletal density of Zn(dcpa) was determined by helium picnometry at 323 K, obtaining a $\rho_s = 1.74 \text{ g/cm}^3$ ($v_s = 1/\rho_s = 0.575 \text{ cm}^3/\text{g}$). For a purely crystalline porous material with a regular lattice, $v_\mu + v_s$ is equal to the specific volume of the unit cell of the lattice. The particle density determined, $\rho_p = 1/(v_s + v_\mu) = 0.957 \text{ g/cm}^3$, is in excellent agreement with the value obtained from the crystallographic data ($\rho_p = 0.961 \text{ g/cm}^3$) by Liu et al. [34].

The adsorption equilibria of CO_2 , CH_4 , and N_2 on the Zn(dcpa) MOF were measured at 273, 303, and 323 K over the pressure range of 0 to 35 bar. The CO_2 , CH_4 , and N_2 absolute adsorption equilibrium isotherms obtained are reported in Figures 5–7, respectively. The CO_2 adsorption isotherms were quite steep in the Henry region, showing a high adsorption capacity at a low pressure, an important feature for use in post-combustion CO_2 capture applications. On the other hand, the N_2 adsorption isotherms were much more linear and had lower adsorption capacity; the CH_4 adsorption isotherms were intermediate between those of CO_2 and N_2 .

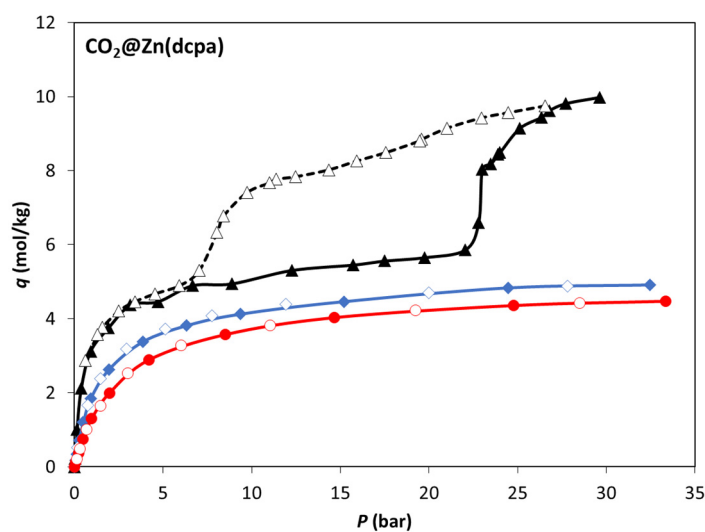


Figure 5. Absolute adsorption equilibrium isotherms of CO₂ on Zn(dcpa) at 273 K (▲), 303 K (◆), and 323 K (●). Filled and empty symbols represent adsorption and desorption experimental data, respectively.

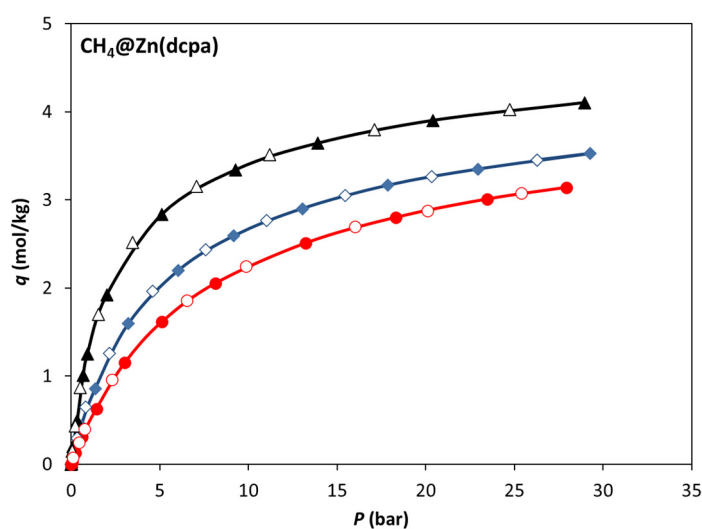


Figure 6. Absolute adsorption equilibrium isotherms of CH₄ on Zn(dcpa) at 273 K (▲), 303 K (◆), and 323 K (●). Filled and empty symbols represent adsorption and desorption experimental data, respectively.

An interesting feature of the CO₂ adsorption equilibrium isotherms can be observed in Figure 5. At 273 K, the adsorption branch of the isotherm follows a typical Langmuir-type shape up to approximately 22 bar, where a step in the isotherm is observed. This behaviour is similar to that observed by Liu et al. [34] for CO₂ adsorption at 195 K, which the authors related to the transition between a shrunken-pore phase and an expanded-pore one. The desorption branch then follows a different path than the adsorption one, showing a hysteresis loop that closes at 7 bar. The reproducibility of this behaviour was checked by repeating the measurements. The stepwise CO₂ adsorption observed is an interesting feature of Zn(dcpa) that can be explored for gas separation or storage applications. It can enhance the working capacity of the solid material upon mild pressure or temperature swings [33]. Despite the observation of the MOF flexibility for CO₂ adsorption at 273 K, the same behaviour was not observed for any of the other temperatures nor for the adsorbate species tested (CH₄ and N₂).

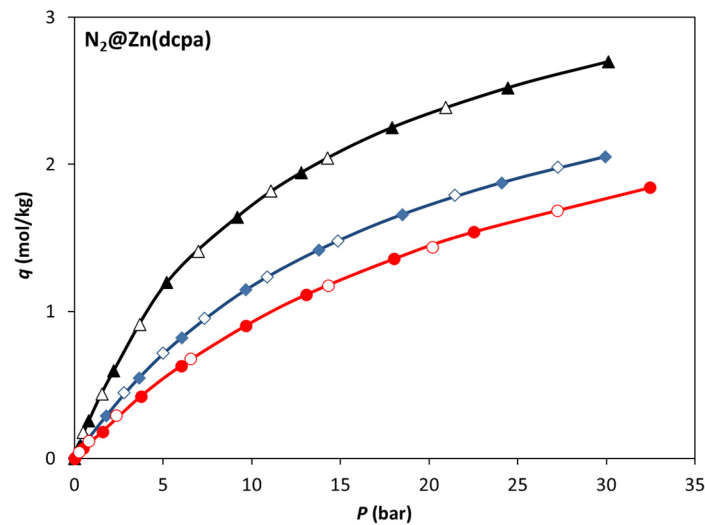


Figure 7. Absolute adsorption equilibrium isotherms of N_2 on Zn(dcpa) at 273 K (\blacktriangle), 303 K (\blacklozenge), and 323 K (\bullet). Filled and empty symbols represent adsorption and desorption experimental data, respectively.

3.3. Osmotic Thermodynamic Theory

Some materials present clear transitions between different metastable framework structures. Zn(dcpa) is an example of such materials. In these cases, an “osmotic subensemble” [15,39–42] can be employed to describe the equilibrium between host structures when exposed to gaseous adsorbates. Alternatively, Ghysels et al. [42] proposed another free energy model able to describe the thermodynamics of breathing phenomena in flexible materials. In this work, we interpreted our data using the former approach.

The osmotic potential [43] of the solid–adsorbate system for the i th structure of Zn(dcpa), either shrunken-pore (SP) or expanded-pore (EP), is

$$\begin{aligned}\Omega_{\text{os}}^{(i)}(P, T) &= F_{\text{host}}^{(i)}(T) + Pv_{\text{p}}^{(i)} - \int_0^P q^{(i)}(P, T)v_{\text{g}}(P, T) dP \\ &= F_{\text{host}}^{(i)}(T) + Pv_{\text{p}}^{(i)} - RT \int_0^P q^{(i)}(P, T)Z(P, T) d \ln P\end{aligned}\quad (3)$$

where $F_{\text{host}}^{(i)}(T)$ corresponds to the empty structure’s free energy at temperature T and $v_{\text{p}}^{(i)}$ to its apparent specific volume (i.e., to the sum of its skeletal, v_{s} , and porous, $v_{\mu}^{(i)}$, volumes); $q^{(i)}(P, T)$ corresponds to the adsorption isotherm considering a rigid framework in its i th structural form; and $v_{\text{g}} = 1/n_{\text{g}}$ and P are the molar volume and compressibility factor of the adsorbative. The difference in the osmotic potential between both of the structures considered (EP and SP), $\Delta\Omega_{\text{os}}(P, T) = \Omega_{\text{os}}^{(\text{EP})}(P, T) - \Omega_{\text{os}}^{(\text{SP})}(P, T)$, is thus

$$\Delta\Omega_{\text{os}}(P, T) = \Delta F_{\text{host}}(T) + P\Delta v_{\text{p}} - RT \int_0^P \Delta q(P, T)Z(P, T) d \ln P\quad (4)$$

where $\Delta\phi \equiv \phi^{(\text{EP})} - \phi^{(\text{SP})}$ is the difference in the value of property ϕ between the EP and SP structures at temperature T . If $\Delta\Omega_{\text{os}} > 0$, the SP structure will be more stable than EP; if $\Delta\Omega_{\text{os}} < 0$, the reverse will be true. For Zn(dcpa), $v_{\mu}^{(\text{EP})} = 0.47 \text{ cm}^3/\text{g}$ and $v_{\mu}^{(\text{SP})} = 0.14 \text{ cm}^3/\text{g}$; hence $\Delta v_{\text{p}} = (v_{\text{s}} + v_{\mu})^{(\text{EP})} - (v_{\text{s}} + v_{\mu})^{(\text{SP})} \approx v_{\mu}^{(\text{EP})} - v_{\mu}^{(\text{SP})} = 0.33 \text{ cm}^3/\text{g}$. Assuming ideal gas behavior ($Z \approx 1$), the previous equation can be simplified to

$$\Delta\Omega_{\text{os}}(P, T) \approx \Delta F_{\text{host}}(T) + P\Delta v_{\text{p}} - RT \int_0^P \Delta q(P, T) d \ln P.\quad (5)$$

If ΔF_{host} and $\Delta q(P)$ are known at a given temperature T , putting $\Delta\Omega_{\text{os}} = 0$ in Equation (4) (or Equation (5)) and solving it for P gives the pressure at which the phase transition occurs at T . However, in real scenarios, the MOF crystals have defects and the

sample has a distribution of crystal sizes, both contributing to smoothing the structural transitions between the two metastable framework structures. Here, we extend the osmotic thermodynamic theory to account for this diffuse effect. It is assumed that for a real sample, ΔF_{host} is normally (Gaussian) distributed around the corresponding value for a perfect crystal with a probability density function

$$f(\Delta F_{\text{host}}) = \frac{1}{\sigma_{\Delta F} \sqrt{2\pi}} \exp\left(-\frac{1}{2} \frac{(\Delta F_{\text{host}} - \Delta F_{\mu})^2}{\sigma_{\Delta F}^2}\right), \quad (6)$$

where ΔF_{μ} is the mean or expectation of the distribution (i.e., the value of ΔF_{host} for a perfect crystal) and $\sigma_{\Delta F}$ is its standard deviation. Given that in the case under study, the structural transition is triggered by exposure to a specific guest species, the previous hypothesis is almost equivalent to considering that the adsorptive pressure, P , that triggers the structural transition at a fixed temperature is also a normally distributed variable and, therefore, that its cumulative distribution function, $\Phi(P)$, at a fixed temperature is

$$\Phi(P) \equiv \int f(P) dP = \frac{1}{2} \left[1 + \operatorname{erf}\left(\frac{P - P_{\mu}}{\sigma_P \sqrt{2}}\right) \right] \quad (7)$$

where P_{μ} is the mean or expectation of the distribution (i.e., the transition pressure for a perfect crystal) and σ_P is its standard deviation. Note that $\Phi(x) = \operatorname{prob}(P \leq x)$, where the right-hand side represents the probability that P takes on a value less than or equal to x . Therefore, the macroscopically observed adsorption branch of the isotherm for a real sample is given by

$$\begin{aligned} q_{\text{ads}}(P) &= [1 - \Phi_{\text{ads}}(P)]q^{(\text{SP})}(P) + \Phi_{\text{ads}}(P)q^{(\text{EP})}(P) \\ q_{\text{des}}(P) &= [1 - \Phi_{\text{des}}(P)]q^{(\text{SP})}(P) + \Phi_{\text{des}}(P)q^{(\text{EP})}(P) \end{aligned} \quad (\text{fixed } T) \quad (8)$$

where $q^{(i)}(P, T)$ is the adsorption isotherm considering a rigid framework constrained to its i th form.

This model was fitted to our experimental data, assuming the adsorption isotherms for the metastable forms of the framework are Langmuirian, i.e.,

$$q^{(i)}(P) = \frac{q_{\infty}^{(i)} b^{(i)} P}{1 + b^{(i)} P} \quad (9)$$

where $q_{\infty}^{(i)}$ and $b^{(i)}$ are the saturation capacity and equilibrium constant for the i th form, respectively, in which case Equation (5) reduces to

$$\Delta \Omega_{\text{os}}(P, T) = \Delta F_{\text{host}}(T) + P \Delta v_p - RT \left[q_{\infty}^{(\text{EP})} \ln(1 + b^{(\text{EP})} P) - q_{\infty}^{(\text{SP})} \ln(1 + b^{(\text{SP})} P) \right] \quad (10)$$

Table 1 lists the parameter values resulting from the model fitting to the experimental data, saturation capacity and Langmuir equilibrium constant ($q_{\infty}^{(i)}$ and $b^{(i)}$) for CO_2 adsorption at 273 K in the SP and EP metastable structures of $\text{Zn}(\text{dcpa})$, mean and standard deviation (P_{μ} and σ_{μ}) of the Gaussian distribution of adsorptive pressure that triggers the phase transition along the adsorption and desorption branches of the isotherm, and the corresponding free energy changes of the empty structure (ΔF_{host}).

Table 1. Fitted parameters of the osmotic thermodynamic theory to the adsorption (Ads) and desorption (Des) branches of the experimental CO₂ isotherm at 273 K. $\Delta F_{\text{host}} \equiv F_{\text{host}}^{(\text{EP})} - F_{\text{host}}^{(\text{SP})}$.

	q_{∞} (mol/kg)	b (atm ⁻¹)		P_{μ} (atm)	σ_P (atm)	ΔF_{host} (J/g)
SP	5.65	1.30	Ads	23.0	1.3	−4.45
EP	12.2	0.143	Des	7.0	0.5	−10.7

Figure 8 compares the experimental adsorption data and the fitted osmotic thermodynamic model, and shows that excellent agreement with the experimental results has been reached using the proposed procedure, substantiated by the fact that the plotted adsorption and desorption curves accurately reproduce the experimental data.

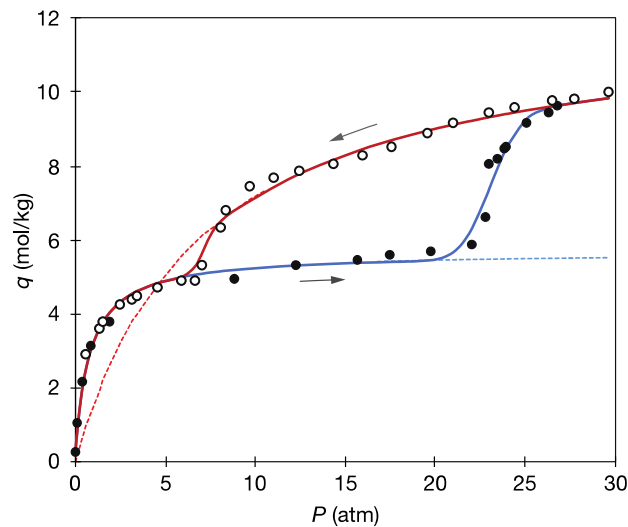


Figure 8. Fitting of the osmotic thermodynamic theory to the adsorption (●) and desorption (○) branches of the experimental CO₂ isotherm at 273 K. Dashed lines: fitted Langmuir adsorption isotherms if the framework were rigid and constrained to its EP (---) and SP (---) forms; solid lines: predicted adsorption (—) and desorption (—) branches of the isotherm at 273 K.

The first two numeric columns of Table 2 list the parameter values of the Langmuir adsorption isotherm model that best fit the CH₄ and N₂ experimental adsorption data at 273 K (Figure 9); these values apply when the framework is in its SP form. The last two columns of Table 2 list the corresponding values if the framework were hypothetically in EP form; given the absence of experimental data, the Langmuir parameters were estimated using the following scaling rules:

$$q_{i,\infty}^{(\text{EP})} = q_{i,\infty}^{(\text{SP})} \frac{q_{\text{CO}_2,\infty}^{(\text{EP})}}{q_{\text{CO}_2,\infty}^{(\text{SP})}} \quad \text{and} \quad b_i^{(\text{EP})} = b_i^{(\text{SP})} \frac{b_{\text{CO}_2}^{(\text{EP})}}{b_{\text{CO}_2}^{(\text{SP})}} \quad (11)$$

Although these rules are rather crude and their application cannot be considered quantitatively precise, they allow us to explain why the adsorption isotherms of CH₄ and N₂ do not point to a phase transition between the SP and EP structures (and no hysteresis) in the pressure range tested experimentally by us. The reason is that in the case of CH₄ or N₂ adsorption, the pressure must be increased considerably, well above the maximum experimental value tested by us, for the term $RT \int_0^P \Delta q(P, T) d \ln P$ to change the sign of $\Delta \Omega_{\text{os}}$. A similar reasoning explains why the CO₂ adsorption isotherms at 303 K and 323 K do not hint at a phase transition between the SP and EP structures.

Table 2. Fitting of the Langmuir adsorption isotherm model to the CH₄ and N₂ experimental adsorption data at 273 K. The parameters for the EP form are estimated as $q_{i,\infty}^{(EP)} = q_{i,\infty}^{(SP)} q_{CO_2,\infty}^{(EP)} / q_{CO_2,\infty}^{(SP)}$ and $b_i^{(EP)} = b_i^{(SP)} b_{CO_2}^{(EP)} / b_{CO_2}^{(SP)}$.

	$q_{\infty}^{(SP)}$ (mol/kg)	$b^{(SP)}$ (atm ⁻¹)	$q_{\infty}^{(EP)}$ (mol/kg)	$b^{(EP)}$ (atm ⁻¹)
N ₂	3.681	0.089	7.948	0.010
CH ₄	4.328	0.411	9.346	0.045

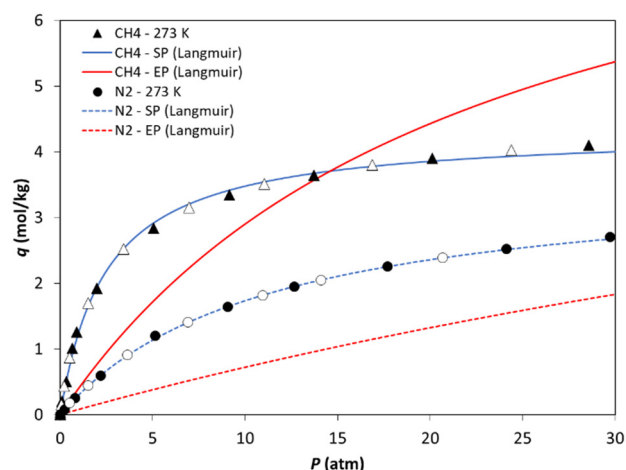


Figure 9. Fitting of the Langmuir isotherm model to the CH₄ (▲) and N₂ (●) experimental adsorption equilibrium isotherms at 273 K. Filled and empty symbols denote experimental adsorption and desorption data, respectively. Solid lines: fitted CH₄ Langmuir isotherm for rigid framework constrained to its EP (red) and SP (blue) forms; dashed lines: fitted N₂ Langmuir isotherm for rigid framework constrained to its EP (red) and SP (blue) forms.

3.4. Potential of Zn(dcpa) for CO₂/N₂ and CO₂/CH₄ Separation

To assess the potential use of Zn(dcpa) for the adsorptive separation of CO₂/N₂ and CO₂/CH₄, we first compared the single-component equilibrium isotherms and the obtained selectivities. Figure 10a compares the isotherms obtained at 303 K for the three gases. The ideal selectivity for an equimolar mixture, $\alpha_{A/B} = q_A/q_B$, was calculated using the single-component adsorption capacity ratio; the obtained results are reported in Figure 10b,c for the CO₂/N₂ and CO₂/CH₄ selectivities, respectively. Both the CO₂/N₂ and CO₂/CH₄ selectivities decreased with the increasing pressure, ranging from 12.8 (at 1 bar) to 6.7 (6 bar) for CO₂/N₂, and from 2.9 (at 1 bar) to 2.1 (6 bar) for CO₂/CH₄. The CO₂/N₂ selectivity was significantly higher than that of CO₂/CH₄, especially at a lower pressure. Although the reported equilibrium selectivity did not take into account the influence of adsorption kinetics or the impact of a real gas mixture, these results serve as a first evaluation of the good potential of Zn(dcpa) for CO₂ separation from CO₂/N₂ and CO₂/CH₄ mixtures. Comparing the selectivity of Zn(dcpa) for CO₂/N₂ with those of the commercial MOFs MIL-53(Al) [31], ZIF-8, [44], and Fe-BTC [45] (Figure 10b,c), it is concluded that the former outperformed the others at a lower pressure. For example, at 1 bar, the order of selectivities was 12.8 (Zn(dcpa)) > 10.5 (Fe-BTC) > 9.6 (MIL-53(Al)) > 5.9 (ZIF-8). The same can be said about the CO₂/CH₄ selectivity trend: 2.9 (Zn(dcpa)) > 2.7 (MIL-53(Al)) > 2.6 (ZIF-8), although in this case, ZIF-8 surpassed Zn(dcpa) at pressures above 2.4 bar.

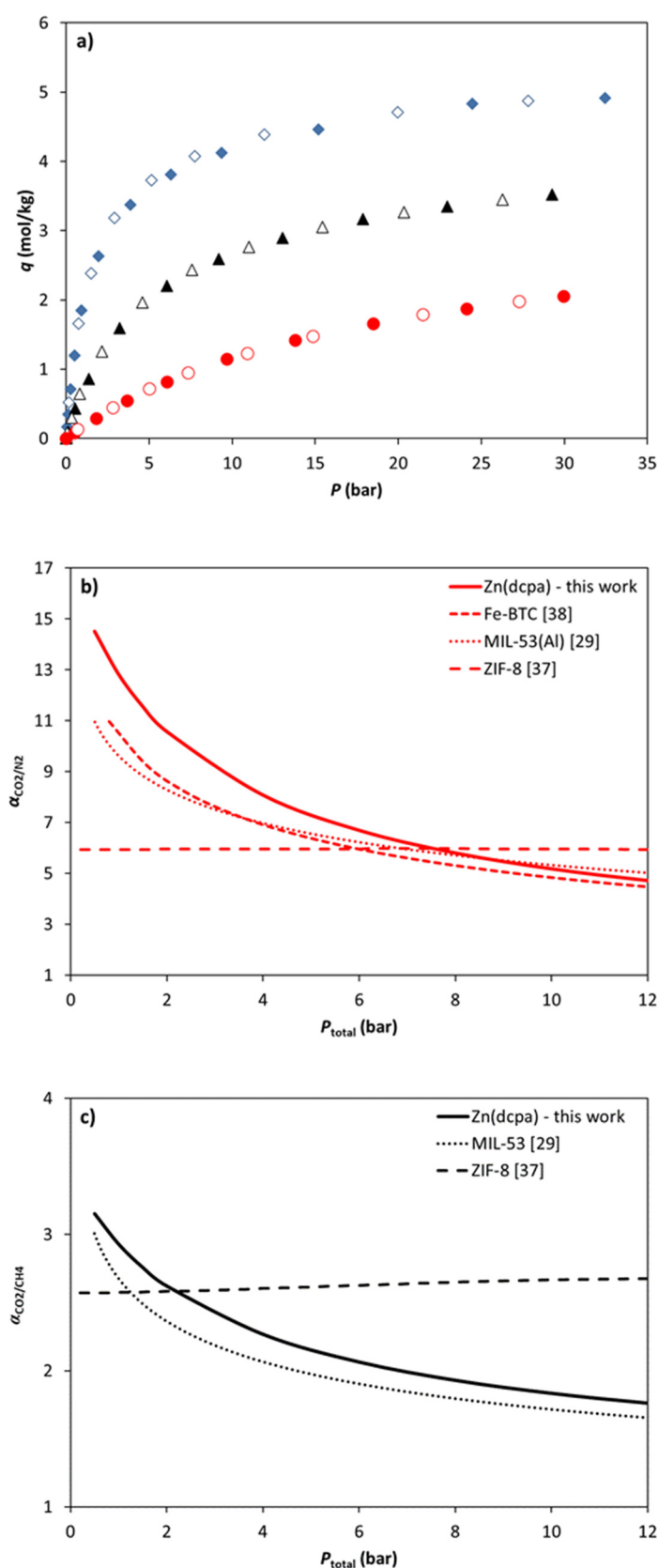


Figure 10. (a) Adsorption equilibrium isotherms of CO_2 (\blacklozenge), CH_4 (\blacktriangle), and N_2 (\bullet) on Zn(dcpa) at 303 K. Filled and empty symbols represent adsorption and desorption data, respectively; (b) CO_2/N_2 and (c) CO_2/CH_4 equilibrium selectivity at 303 K as a function of pressure for Zn(dcpa) and commercial MOFs MIL-53(Al) [31], ZIF-8 [44], and Fe-BTC [45].

The isosteric heat of adsorption, Q_{st} , was determined from the experimental data via the Clausius–Clapeyron equation: $(\log P)_q = \text{const} - Q_{st}/RT$ [46]. Using this approach, the plot of $\log P$ versus $-1/RT$, at constant loading, should give a straight line from which the slope of Q_{st} can be obtained. The plots in Figure 11 of Q_{st} for CO_2 , CH_4 , and N_2 on $\text{Zn}(\text{dcpa})$ as a function of loading show that for CH_4 , their values were approximately constant within the loading range studied, while for CO_2 and N_2 , a linear increase was observed. It should be noted that in the case of CO_2 , Q_{st} was plotted for loadings lower than the MOF's conformational change observed at 273 K, i.e., less than 4 mol/kg. The isosteric heat of the adsorption was higher for CO_2 (23–28 kJ/mol), which is in accordance with the values reported in the literature [34], followed by that for CH_4 (~19.5 kJ/mol) and N_2 (13–15 kJ/mol).

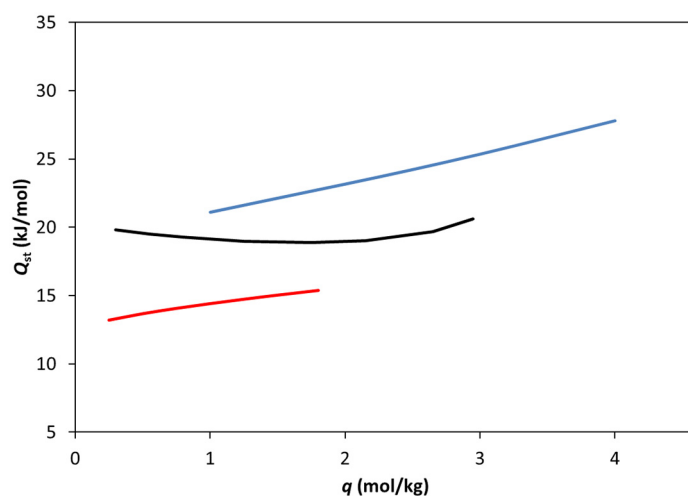


Figure 11. CO_2 (blue), CH_4 (black), and N_2 (red) isosteric heats of adsorption, Q_{st} , as a function of loading, q .

4. Conclusions

$\text{Zn}(\text{dcpa})$ MOF was characterized through PXRD, thermogravimetric analysis, and N_2 adsorption at 77 K. In line with the XRD and N_2 data reported by Liu et al. [34], our results indicate that the framework conformation changes (pore shrinkage/pore expansion) upon removal/loading of guest molecules. The TGA results demonstrate that the MOF is stable up to 650 K.

The adsorption equilibrium isotherms of CO_2 , CH_4 , and N_2 on $\text{Zn}(\text{dcpa})$ at 273 K, 303 K, and 323 K are reported up to 35 bar. The obtained data highlight the interesting behavior of CO_2 adsorption at 273 K, which exhibits a stepped isotherm related to the transition between shrunken- and expanded-pore phases at around 22 bar. When observing the desorption branch of the isotherm, a hysteresis loop is present, closing at 7 bar. Although the same behavior is observed for CO_2 adsorption at 195 K [34], this is the first report of this effect at 273 K. None of the remaining CO_2 (303 K and 323 K), CH_4 , or N_2 isotherms show the same behavior.

The CO_2 adsorption equilibrium at 273 K is accurately interpreted using the osmotic thermodynamic theory, which is further refined by considering that the free energy difference between the two metastable structures of $\text{Zn}(\text{dcpa})$ is a normally distributed variable due to the distribution of crystal sizes and the defects in a real MOF sample.

Regarding the uptake amounts, $\text{Zn}(\text{dcpa})$ can adsorb higher amounts of CO_2 , followed by CH_4 and N_2 . The CO_2/N_2 and CO_2/CH_4 ideal equilibrium selectivities of $\text{Zn}(\text{dcpa})$ at 303 K are evaluated for equimolar mixtures, resulting in 12.8 and 2.9, respectively, for a total pressure of 1 bar.

The reported data are essential for the modelling of adsorption-based processes, namely pressure swing adsorption (PSA) and temperature swing adsorption (TSA), for the separation of mixtures containing the studied gases, e.g., biogas upgrading and CO₂ capture from flue gases.

Author Contributions: Conceptualization, R.P.P.L.R. and J.P.B.M.; formal analysis, R.P.P.L.R. and J.P.B.M.; investigation, R.P.P.L.R. and I.A.A.C.E.; writing—original draft preparation, R.P.P.L.R.; writing—review and editing, R.P.P.L.R., I.A.A.C.E. and J.P.B.M.; visualization, R.P.P.L.R. and J.P.B.M. All authors have read and agreed to the published version of the manuscript.

Funding: This research was funded by the Associate Laboratory for Green Chemistry (AQV), which is financed by national funds from FCT/MCTES (UIDB/50006/2020 and UIDP/50006/2020). Rui Ribeiro and Isabel Esteves acknowledge financial support from FCT/MCTES through the Norma Transitória DL 57/2016 Program Contract and project IF/01016/2014, respectively. The authors also acknowledge support from the ERANet LAC initiative through project ELAC2014/BEE0367.

Conflicts of Interest: The authors declare no conflict of interest. The funders had no role in the design of the study; in the collection, analyses, or interpretation of data; in the writing of the manuscript; or in the decision to publish the results.

References

1. Herm, Z.R.; Swisher, J.A.; Smit, B.; Krishna, R.; Long, J.R. Metal-organic frameworks as adsorbents for hydrogen purification and precombustion carbon dioxide capture. *J. Am. Chem. Soc.* **2011**, *133*, 5664–5667. [[CrossRef](#)] [[PubMed](#)]
2. Grande, C.A.; Blom, R.; Andreassen, K.A.; Stensrød, R.E. Experimental results of pressure swing adsorption (PSA) for pre-combustion CO₂ capture with metal organic frameworks. *Energy Procedia* **2017**, *114*, 2265–2270. [[CrossRef](#)]
3. Rowsell, J.L.C.; Yaghi, O.M. Metal-organic frameworks: A new class of porous materials. *Micropor. Mesopor. Mat.* **2004**, *73*, 3–14. [[CrossRef](#)]
4. Férey, G. Hybrid porous solids: Past, present, future. *Chem. Soc. Rev.* **2008**, *37*, 191–214. [[CrossRef](#)] [[PubMed](#)]
5. Millward, A.R.; Yaghi, O.M. Metal-organic frameworks with exceptionally high capacity for storage of carbon dioxide at room temperature. *J. Am. Chem. Soc.* **2005**, *127*, 17998–17999. [[CrossRef](#)]
6. Furukawa, H.; Cordova, K.E.; O’Keeffe, M.; Yaghi, O.M. The chemistry and applications of metal-organic frameworks. *Science* **2013**, *341*. [[CrossRef](#)]
7. Czaja, A.U.; Trukhan, N.; Muller, U. Industrial applications of metal-organic frameworks. *Chem. Soc. Rev.* **2009**, *38*, 1284–1293. [[CrossRef](#)] [[PubMed](#)]
8. Meek, S.T.; Greathouse, J.A.; Allendorf, M.D. Metal-organic frameworks: A rapidly growing class of versatile nanoporous materials. *Adv. Mater.* **2011**, *23*, 249–267. [[CrossRef](#)]
9. Mueller, U.; Schubert, M.; Teich, F.; Puetter, H.; Schierle-Arndt, K.; Pastre, J. Metal-organic frameworks—Prospective industrial applications. *J. Mater. Chem.* **2006**, *16*, 626–636. [[CrossRef](#)]
10. Ribeiro, R.P.P.L.; Antunes, C.L.; Garate, A.U.; Portela, A.F.; Plaza, M.G.; Mota, J.P.B.; Esteves, I.A.A.C. Binderless shaped metal-organic framework particles: Impact on carbon dioxide adsorption. *Microporous Mesoporous Mater.* **2019**, *275*, 111–121. [[CrossRef](#)]
11. An, Y.; Tian, Y.; Li, Y.; Wei, C.; Tao, Y.; Liu, Y.; Xi, B.; Xiong, S.; Feng, J.; Qian, Y. Heteroatom-doped 3D porous carbon architectures for highly stable aqueous zinc metal batteries and non-aqueous lithium metal batteries. *Chem. Eng. J.* **2020**, *400*, 125843. [[CrossRef](#)]
12. An, Y.; Tian, Y.; Li, Y.; Xiong, S.; Zhao, G.; Feng, J.; Qian, Y. Green and tunable fabrication of graphene-like N-doped carbon on a 3D metal substrate as a binder-free anode for high-performance potassium-ion batteries. *J. Mater. Chem. A* **2019**, *7*, 21966–21975. [[CrossRef](#)]
13. Alhamami, M.; Doan, H.; Cheng, C.-H. A review on breathing behaviors of metal-organic-frameworks (MOFs) for gas adsorption. *Materials* **2014**, *7*, 3198–3250. [[CrossRef](#)]
14. Schneemann, A.; Bon, V.; Schwedler, I.; Senkowska, I.; Kaskel, S.; Fischer, R.A. Flexible metal-organic frameworks. *Chem. Soc. Rev.* **2014**, *43*, 6062–6096. [[CrossRef](#)]
15. Coudert, F.-X.; Mellot-Draznieks, C.; Fuchs, A.H.; Boutin, A. Double structural transition in hybrid material MIL-53 upon hydrocarbon adsorption: The thermodynamics behind the scenes. *J. Am. Chem. Soc.* **2009**, *131*, 3442–3443. [[CrossRef](#)] [[PubMed](#)]
16. Mishra, P.; Edubilli, S.; Uppara, H.P.; Mandal, B.; Gumma, S. Effect of adsorbent history on adsorption characteristics of MIL-53 (Al) metal organic framework. *Langmuir* **2013**, *29*, 12162–12167. [[CrossRef](#)] [[PubMed](#)]
17. Serre, C.; Millange, F.; Thouvenot, C.; Noguès, M.; Marsolier, G.; Louër, D.; Férey, G. Very large breathing effect in the first nanoporous chromium (III)-based solids: MIL-53 or Cr^{III}(OH)·{O₂C–C₆H₄–CO₂}·{[HO₂C–C₆H₄–CO₂H]_x·H₂O_y}. *J. Am. Chem. Soc.* **2002**, *124*, 13519–13526. [[CrossRef](#)]
18. Fairen-Jimenez, D.; Galvelis, R.; Torrisi, A.; Gellan, A.D.; Wharmby, M.T.; Wright, P.A.; Mellot-Draznieks, C.; Duren, T. Flexibility and swing effect on the adsorption of energy-related gases on ZIF-8: Combined experimental and simulation study. *Dalton Trans.* **2012**, *41*, 10752–10762. [[CrossRef](#)] [[PubMed](#)]

19. Fairen-Jimenez, D.; Moggach, S.A.; Wharmby, M.T.; Wright, P.A.; Parsons, S.; Düren, T. Opening the gate: Framework flexibility in ZIF-8 explored by experiments and simulations. *J. Am. Chem. Soc.* **2011**, *133*, 8900–8902. [[CrossRef](#)]
20. Loiseau, T.; Serre, C.; Huguenard, C.; Fink, G.; Taulelle, F.; Henry, M.; Bataille, T.; Férey, G. A rationale for the large breathing of the porous aluminum terephthalate (MIL-53) upon hydration. *Chem. Eur. J.* **2004**, *10*, 1373–1382. [[CrossRef](#)] [[PubMed](#)]
21. Hamon, L.; Serre, C.; Devic, T.; Loiseau, T.; Millange, F.; Férey, G.; Weireld, G.D. Comparative study of hydrogen sulfide adsorption in the MIL-53 (Al, Cr, Fe), MIL-47 (V), MIL-100 (Cr), and MIL-101 (Cr) metal-organic frameworks at room temperature. *J. Am. Chem. Soc.* **2009**, *131*, 8775–8777. [[CrossRef](#)]
22. Chen, L.; Mowat, J.P.S.; Fairen-Jimenez, D.; Morrison, C.A.; Thompson, S.P.; Wright, P.A.; Düren, T. Elucidating the breathing of the metal-organic framework MIL-53 (Sc) with ab initio molecular dynamics simulations and in situ X-ray powder diffraction experiments. *J. Am. Chem. Soc.* **2013**, *135*, 15763–15773. [[CrossRef](#)] [[PubMed](#)]
23. Boutin, A.; Coudert, F.X.; Springuel-Huet, M.A.; Neimark, A.V.; Férey, G.; Fuchs, A.H. The behavior of flexible MIL-53 (Al) upon CH₄ and CO₂ adsorption. *J. Phys. Chem. C* **2010**, *114*, 22237–22244. [[CrossRef](#)]
24. Liu, Y.; Her, J.-H.; Dailly, A.; Ramirez-Cuesta, A.J.; Neumann, D.A.; Brown, C.M. Reversible structural transition in MIL-53 with large temperature hysteresis. *J. Am. Chem. Soc.* **2008**, *130*, 11813–11818. [[CrossRef](#)] [[PubMed](#)]
25. Beurroies, I.; Boulhout, M.; Llewellyn, P.L.; Kuchta, B.; Férey, G.; Serre, C.; Denoyel, R. Using pressure to provoke the structural transition of metal-organic frameworks. *Angew. Chem. Int. Ed.* **2010**, *49*, 7526–7529. [[CrossRef](#)]
26. Neimark, A.V.; Coudert, F.-X.; Triguero, C.; Boutin, A.; Fuchs, A.H.; Beurroies, I.; Denoyel, R. Structural transitions in MIL-53 (Cr): View from outside and inside. *Langmuir* **2011**, *27*, 4734–4741. [[CrossRef](#)]
27. Serre, C.; Bourrelly, S.; Vimont, A.; Ramsahye, N.A.; Maurin, G.; Llewellyn, P.L.; Daturi, M.; Filinchuk, Y.; Leynaud, O.; Barnes, P.; et al. An explanation for the very large breathing effect of a metal-organic framework during CO₂ adsorption. *Adv. Mater.* **2007**, *19*, 2246–2251. [[CrossRef](#)]
28. Mounfield, W.P., III; Walton, K.S. Effect of synthesis solvent on the breathing behavior of MIL-53 (Al). *J. Colloid Interface Sci.* **2015**, *447*, 33–39. [[CrossRef](#)]
29. Heymans, N.; Vaesen, S.; De Weireld, G. A complete procedure for acidic gas separation by adsorption on MIL-53 (Al). *Microporous Mesoporous Mater.* **2012**, *154*, 93–99. [[CrossRef](#)]
30. Deniz, E.; Karadas, F.; Patel, H.A.; Aparicio, S.; Yavuz, C.T.; Atilhan, M. A combined computational and experimental study of high pressure and supercritical CO₂ adsorption on Basolite MOFs. *Microporous Mesoporous Mater.* **2013**, *175*, 34–42. [[CrossRef](#)]
31. Camacho, B.C.R.; Ribeiro, R.P.P.L.; Esteves, I.A.A.C.; Mota, J.P.B. Adsorption equilibrium of carbon dioxide and nitrogen on the MIL-53 (Al) metal organic framework. *Sep. Purif. Technol.* **2015**, *141*, 150–159. [[CrossRef](#)]
32. Gonzalez-Nelson, A.; Coudert, F.X.; van der Veen, M.A. Rotational dynamics of linkers in metal-organic frameworks. *Nanomaterials* **2019**, *9*, 330. [[CrossRef](#)]
33. Hefti, M.; Joss, L.; Bjelobrk, Z.; Mazzotti, M. On the potential of phase-change adsorbents for CO₂ capture by temperature swing adsorption. *Faraday Discuss.* **2016**, *192*, 153–179. [[CrossRef](#)]
34. Liu, B.; Li, Y.; Hou, L.; Yang, G.; Wang, Y.Y.; Shi, Q.-Z. Dynamic Zn-based metal-organic framework: Step wise adsorption, hysteretic desorption and selective carbon dioxide uptake. *J. Mater. Chem.* **2013**, *1*, 6535–6538. [[CrossRef](#)]
35. Ribeiro, R.P.P.L.; Barreto, J.; GrossoXavier, M.D.; Martins, D.; Esteves, I.A.A.C.; Branco, M.; Tirolien, T.; Mota, J.P.B.; Bonfait, G. Cryogenic neon adsorption on Co₃(ndc)₃(dabco) metal-organic framework. *Microporous and Mesoporous Mater.* **2020**, *298*, 110055. [[CrossRef](#)]
36. Lyubchyk, A.; Esteves, I.A.A.C.; Cruz, F.J.A.L.; Mota, J.P.B. Experimental and theoretical studies of supercritical methane adsorption in the MIL-53 (Al) metal organic framework. *J. Phys. Chem.* **2011**, *115*, 20628–20638. [[CrossRef](#)]
37. Ribeiro, R.P.P.L.; Camacho, B.C.R.; Lyubchyk, A.; Esteves, I.A.A.C.; Cruz, F.J.A.L.; Mota, J.P.B. Experimental and computational study of ethane and ethylene adsorption in the MIL-53 (Al) metal organic framework. *Microporous and Mesoporous Mater.* **2016**, *230*, 154–165. [[CrossRef](#)]
38. Dreisbach, F.; Staudt, R.; Keller, J.U. High pressure adsorption data of methane, nitrogen, carbon dioxide and their binary and ternary mixtures on activated carbon. *Adsorption* **1999**, *5*, 215–227. [[CrossRef](#)]
39. Coudert, F.-X.; Jeffroy, M.; Fuchs, A.H.; Boutin, A.; Mellot-Draznieks, C. Thermodynamics of guest-induced structural transitions in hybrid organic-inorganic frameworks. *J. Am. Chem. Soc.* **2008**, *130*, 14294–14302. [[CrossRef](#)] [[PubMed](#)]
40. Mota, J.P.B.; Martins, D.; Lopes, D.; Catarino, I.; Bonfait, G. Structural transitions in the MIL-53 (Al) metal-organic framework upon cryogenic hydrogen adsorption. *J. Phys. Chem.* **2017**, *121*, 24252–24263. [[CrossRef](#)]
41. Hiraide, S.; Sakanaka, Y.; Kajiro, H.; Kawaguchi, S.; Miyahara, M.T.; Tanaka, H. High-through put gas separation by flexible metal-organic frameworks with fast gating and thermal management capabilities. *Nat. Commun.* **2020**, *11*, 3867. [[CrossRef](#)]
42. Ghysels, A.; Vanduyfhuys, L.; Vandichel, M.; Waroquier, M.; Van Speybroeck, V.; Smit, B. On the thermodynamics of framework breathing: A free energy model for gas adsorption in MIL-53. *J. Phys. Chem.* **2013**, *117*, 11540–11554. [[CrossRef](#)]
43. Jeffroy, M.; Fuchs, A.H.; Boutin, A. Structural changes in nanoporous solids due to fluid adsorption: Thermodynamic analysis and Monte Carlo simulations. *Chem. Commun.* **2008**, 3275–3277. [[CrossRef](#)] [[PubMed](#)]
44. Ferreira, T.J.; Vera, A.T.; De Moura, B.A.; Esteves, L.M.; Tariq, M.; Esperança, J.M.S.S.; Esteves, I.A.A.C. Paramagnetic ionic liquid/metal organic framework composites for CO₂/CH₄ and CO₂/N₂ separations. *Front. Chem.* **2020**, *8*, 590191. [[CrossRef](#)] [[PubMed](#)]

-
45. Nabais, A.R.; Ribeiro, R.P.P.L.; Mota, J.P.B.; Alves, V.D.; Esteves, I.A.A.C.; Neves, L.A. CO₂/N₂ gas separation using Fe (BTC)-based mixed matrix membranes: A view on the adsorptive and filler properties of metal-organic frameworks. *Sep. Purif. Technol.* **2018**, *202*, 174–184. [[CrossRef](#)]
 46. Poling, B.E.; Prausnitz, J.M.; O'Connell, J.P. *The Properties of Gases and Liquids*; McGraw-Hill: New York, NY, USA, 2001.